J. Fluid Mech. (2009), *vol.* 619, *pp.* 235–259. © 2008 Cambridge University Press
doi:10.1017/S0022112008004503 Printed in the United Kingdom

The tidally induced bottom boundary layer in the rotating frame: development of the turbulent mixed layer under stratification

KEI SAKAMOTO[1,2]† AND KAZUNORI AKITOMO[3]

[1]Oceanographic Research Department, Meteorological Research Institute, Tsukuba, Japan

[2]Center for Climate System Research, University of Tokyo, Kashiwa, Japan

[3]Department of Geophysics, Graduate School of Science, Kyoto University, Kyoto, Japan

(Received 14 December 2007 and in revised form 9 September 2008)

To investigate turbulent properties and the developing mechanisms of the tidally induced bottom boundary layer in the linearly stratified ocean, numerical experiments have been executed with a non-hydrostatic three-dimensional model in the rotating frame, changing the temporal Rossby number $Ro_t = |\sigma/f|$, i.e. the ratio of the tidal frequency σ to the Coriolis parameter f. After the flow transitions to turbulence, the entire water column can be characterized by three layers: the mixed layer where density is homogenized and the flow is turbulent ($z < z_m$); the stratified layer where the initial stratification remains and the flow is laminar ($z > z_t$); and the interfacial layer between them where the flow is turbulent but the stratification remains ($z_m < z < z_t$). Turbulence is scaled by the frictional velocity u_τ and the mixed-layer thickness z_m (u_τ and u_τ/N where N is the buoyancy frequency) in the mixed (interfacial) layer, and has similarity. The mixed layer is thickened by the process where light water of the upper stratified layer is mixed with the lower unstratified layer water through the interfacial layer. As Ro_t approaches unity, i.e. near the critical latitude, the mixed layer develops more rapidly according to the following mechanism. As becomes Ro_t closer to unity, the current shear in the interfacial layer is intensified, since the difference of velocity becomes larger between the lower turbulent mixed and upper laminar stratified layers, and this leads to thickening of the interfacial layer. As a result, density deviation of the water entrained from above becomes larger, and this causes more rapid development of the mixed layer. In terms of the energy conversion from the eddy kinetic energy (EKE) to the potential energy (PE), the efficiency factor β which is the ratio of the conversion rate from EKE to PE to that from the tidal shear to EKE increased from 0.25 % for $Ro_t = 0.5$ to 3.5 % for $Ro_t = 1.05$ on average. When the time is normalized by the period required for the mixed layer to be thickened to the unstratified turbulent boundary layer $\delta = u_\tau/|f + \sigma|$, the mixed layer development occurred in a similar manner in all cases. This similarity suggests the possibility of universal formulation for the turbulent tidal mixing under stratification.

1. Introduction

Tidal currents can dominate the current regime over large parts of shallow coastal regions and continental shelves, and can play an important role in vertical mixing and

† Email address for correspondence: ksakamot@mri-jma.go.jp

determination of water properties. Shear instability as well as the breaking of internal tides is a dominant mechanism for turbulent mixing (Robertson 2001*a*, *b*; Chen, Ou & Dong 2003). The so-called tidal front which is formed between shallow mixed and deep stratified regions in summer is a representative case in which shear instability plays a dominant role in the tidally induced bottom boundary layer (TBBL) (e.g. Yanagi & Koike 1987; Guo & Valle-Levinson 2007). Turbulent mixing in the TBBL also makes a contribution to bioproduction in the shallow coastal regions by transporting water with abundant nutrients near the bottom upward to the photic layer (Furevik & Foldvik 1996). The water environment is also affected through sediment erosion and transport due to turbulence in the TBBL (Chen, Ling & Gartner 1999).

Turbulent mixing in the TBBL is largely affected by the latitude. As the frequency of tides approaches that of the Coriolis parameter, the boundary layer becomes thicker. The thick well-mixed layer has been observed on the continental shelves of Antarctica (Gordon 1998; Whitworth *et al.* 1998; Foldvik *et al.* 2004) and the Barents Sea (Furevik & Foldvik 1996), and this has been attributed to the thickened TBBL because the frequency of semi-diurnal tides is close to the Coriolis parameter in the polar oceans (Foster, Foldvik & Middleton 1987; Pereira *et al.* 2002). However, most previous studies discussed the role of the TBBL based on the theory of the laminar flow (constant viscosity) or assumed profiles of turbulent viscosity (Foldvik, Middelton & Foster 1990; Nost 1994; Robertson 2001*a*; Pereira *et al.* 2002).

Instability and turbulence of the TBBL in the rotating frame have been investigated by Aelbrecht, D'Hieres & Renouard (1999), Sakamoto & Akitomo (2006), and Sakamoto & Akitomo (2008) (referred to as SA08 hereinafter) with laboratory or numerical experiments. For the TBBL under the unstratified condition, SA08 showed that turbulent properties have similarity by introducing the modified 'outer scales', i.e. velocity scale of u_τ, time scale of $|f+\sigma|^{-1}$ and length scale of $\delta = u_\tau/|f+\sigma|$, where u_τ, σ and f are the frictional velocity, the tidal frequency and the Coriolis parameter, respectively, as in the turbulent Ekman flow (Tennekes & Lumley 1972; Coleman 1999). Also, considering the M2 tide with amplitude of 8.4×10^{-2} m s^{-1} near the critical latitude (an experiment with the temporal Rossby number $Ro_t = |\sigma/f|$ of 1.05), SA08 showed that the vertical scale of the TBBL (δ) reached 440 m and the apparent diffusivity was evaluated at up to 0.06 m^2 s^{-1}. This result is consistent with the observations implying that active mixing occurs on polar shelves, since the critical latitude of the M2 tide is 74.5°.

SA08 excluded stratification, which may work as another important factor for mixing processes in the ocean. It suppresses turbulent motion and changes the vertical structure of the tidal current (e.g. Werner *et al.* 2003; Makinson, Schröder & Østerhus 2006). Further, development of the bottom boundary (mixed) layer through the energy conversion from the kinetic energy to the potential energy of the water column is crucial to coastal phenomena such as tidal fronts (e.g. Simpson & Hunter 1974). However, the detailed process of the turbulent energy conversion has not yet been thoroughly clarified.

In recent years, turbulent closure models such as proposed by Mellor & Yamada (1982) (MY scheme) have been widely used for evaluation of turbulent mixing in the TBBL. Makinson (2002) executed a numerical experiment of the TBBL in the polar ocean using a vertical one-dimensional model embodied with the MY scheme, and found that turbulent mixing is intensified near the critical latitude where the tidal frequency coincides with the Coriolis parameter. Werner *et al.* (2003) succeeded in reproducing the vertical structure of the tidal current using the MY scheme. However, the MY scheme does not necessarily provide satisfactory results under

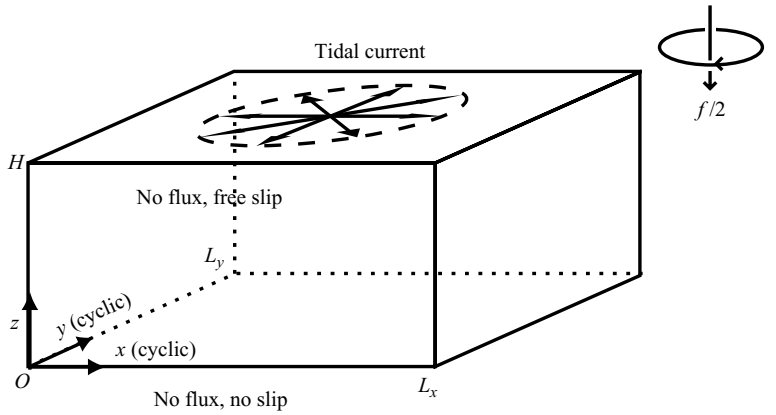

FIGURE 1. Model basin and the coordinate system with boundary conditions.

strong stratification (Nunes Vaz & Simpson 1994; Werner *et al.* 2003). While the modified length scale given by q/N (q: velocity scale of turbulence, and N: the buoyancy frequency) improved the performance of the scheme (Burchard, Petersen & Rippeth 1998; Burchard 2001; Nakanishi 2001), the modification has no robust basis from observations or experiments, and adequate results could not be obtained in some cases, even if this modification was adopted (Li, Zhong & Boicourt 2005; Warner, Geyer & Lerczak 2005).

In this study, we investigate turbulent properties in the stratified TBBL and the basic mechanism of the bottom mixed-layer development, by directly simulating turbulent motions with a non-hydrostatic three-dimensional numerical model (DNS). A schematic view of conclusions obtained here is presented at the end of the paper (figure 15).

2. Numerical model

Numerical experiments were executed with the same model configuration as in SA08 except for introducing density stratification. The model basin is rectangular of size $L_x \times L_y \times H$ (figure 1). The origin of the coordinate system is placed at the bottom. The x- and y-axes are set horizontal, and the z-axis is directed upward. The background tidal current $\boldsymbol{u}_{tide} = (u_{tide}, v_{tide}, 0)$ was imposed as the model forcing, instead of the tidal sea surface elevation, to focus on the turbulent boundary layer induced by the tidal current (e.g. Akhavan, Kamm & Shapiro 1991). The corresponding tidal elevation is too small to affect the results (see SA08 for a detailed explanation). The governing equations of the model are the non-hydrostatic momentum and continuity equations for the velocity deviation $\boldsymbol{u} = (u, v, w)$ from $\boldsymbol{u}_{tide}$, and the advection–diffusion equation of density under the Boussinesq and rigid-lid approximations,

$$\frac{\partial \boldsymbol{u}}{\partial t} + (\boldsymbol{u}_{tide} \cdot \nabla)\boldsymbol{u} + (\boldsymbol{u} \cdot \nabla)\boldsymbol{u}_{tide} + (\boldsymbol{u} \cdot \nabla)\boldsymbol{u} + f\boldsymbol{z} \times \boldsymbol{u} = -\frac{1}{\rho_0}\nabla p - z\frac{\rho}{\rho_0}g + \nu\nabla^2\boldsymbol{u}, \quad (2.1)$$

$$\nabla \cdot \boldsymbol{u} = 0, \quad (2.2)$$

$$\frac{\partial \rho}{\partial t} + (\boldsymbol{u}_{tide} \cdot \nabla)\rho + (\boldsymbol{u} \cdot \nabla)\rho = \kappa\nabla^2\rho. \quad (2.3)$$

The variable p is the pressure deviation from the hydrostatic balance, and ρ the deviation from the reference density ρ_0 ($1.027 \times 10^3\,\mathrm{kg\,m^{-3}}$). z is the unit vector in the z-direction. The constants g and f are the acceleration due to gravity ($9.8\,\mathrm{m\,s^{-2}}$) and the Coriolis parameter (negative for the southern hemisphere), respectively. The viscosity ν and diffusivity κ were set to $1 \times 10^{-4}\,\mathrm{m^2\,s^{-1}}$, which was as small as possible in the range in which we could execute the present model (DNS) under the limited computer resources.

While the periodic condition was imposed in the horizontal direction ($x = 0$, L_x and $y = 0$, L_y), no-slip and free-slip conditions were imposed at the bottom ($z = 0$) and the rigid sea surface ($z = H$), respectively,

$$u = v = w = 0 \qquad \text{at} \quad z = 0, \tag{2.4}$$

$$\frac{\partial u}{\partial z} = \frac{\partial v}{\partial z} = w = 0 \qquad \text{at} \quad z = H. \tag{2.5}$$

No density flux was imposed at the vertical boundaries,

$$\frac{\partial \rho}{\partial z} = 0 \qquad \text{at} \quad z = 0, H. \tag{2.6}$$

Assuming the temporally oscillating pressure gradient in the x-direction, the background tidal current $\boldsymbol{u}_{tide}$ was analytically determined with constant ν as in SA08,

$$\begin{aligned} & u_{tide}(z,t) + \mathrm{i}v_{tide}(z,t) \\ &= \begin{cases} U_{tide}\dfrac{f-\sigma}{2f}\exp(\mathrm{i}\sigma t)\left(1-\exp\left(-\dfrac{(1-\mathrm{i})z}{\sqrt{2\nu/|f+\sigma|}}\right)\right) \\ \quad + U_{tide}\dfrac{-f-\sigma}{2f}\exp(\mathrm{i}\sigma t)\left(1-\exp\left(-\dfrac{(1-\mathrm{i})z}{\sqrt{2\nu/|f-\sigma|}}\right)\right) & \text{for } |f| > \sigma, \\ U_{tide}\dfrac{-f+\sigma}{2\sigma}\exp(\mathrm{i}\sigma t)\left(1-\exp\left(-\dfrac{(1+\mathrm{i})z}{\sqrt{2\nu/|f+\sigma|}}\right)\right) \\ \quad + U_{tide}\dfrac{f+\sigma}{2\sigma}\exp(\mathrm{i}\sigma t)\left(1-\exp\left(-\dfrac{(1-\mathrm{i})z}{\sqrt{2\nu/|f-\sigma|}}\right)\right) & \text{for } |f| < \sigma, \end{cases} \end{aligned} \tag{2.7}$$

where σ and U_{tide} are the frequency and amplitude, respectively (see Appendix A of Sakamoto & Akitomo (2006) for derivation). The vertical scale of $\boldsymbol{u}_{tide}$ is given by $H_{tide} = \sqrt{2\nu/|f+\sigma|}$, and πH_{tide} corresponds to the thickness of the laminar viscous boundary layer.

In this study, we assumed that σ and U_{tide} were fixed at $1.45 \times 10^{-4}\,\mathrm{s^{-1}}$ (semi-diurnal tide) and $8.5\,\mathrm{cm\,s^{-1}}$, respectively. As in SA08, six cases A to F were executed changing the temporal Rossby number $Ro_t = |\sigma/f|$ from 0.5 to 2.0, together with two extreme cases, an Ekman flow (case Ek, $Ro_t = 0$) which is induced by a steady flow in a rotating frame, and a Stokes flow (St, $Ro_t \to \infty$) which is induced by an oscillating flow in a non-rotating frame (table 1). For semi-diurnal tides, cases D, E and F correspond to the latitude of 72 °S, 56 °S and 30 °S, respectively. Although cases A, B and C do not have corresponding latitudes on the Earth for semi-diurnal tides, they correspond to the latitude of 90 °S, 39 °S and 32 °S, respectively, for diurnal tides. For comparison, additional cases E′ and E″ for $Ro_t = 1.2$ were executed with doubled and halved U_{tide}, i.e. $17.1\,\mathrm{cm\,s^{-1}}$ and $4.3\,\mathrm{cm\,s^{-1}}$, respectively.

The interior current vector $\boldsymbol{u}_{int}$ (free of viscous effect) given by

$$\boldsymbol{u}_{int}(t) = \lim_{z \to \infty} \boldsymbol{u}_{tide}(z,t), \tag{2.8}$$

Case	Ek	A	B	C	D	E	F	St
$Ro_t(=\lvert\sigma/f\rvert)$	0	0.5	0.8	0.95	1.05	1.2	2.0	∞
latitude for semi-diurnal tides	—	—	—	—	72°S	56°S	30°S	0°
$H_{tide}(=\sqrt{2\nu/\lvert f+\sigma\rvert})$ [m]	1.2	1.2	2.4	5.1	5.4	2.9	1.7	1.2
$Re(=H_{tide}U_{tide}/\nu)$	1000	1000	2000	4400	4600	2500	1400	1000
$u_\tau=(\sqrt{\lvert\boldsymbol{\tau}_{btm}\rvert/\rho_0})$ $[\times10^{-3}\,\mathrm{m\,s^{-1}}]$	4.7	3.8	3.7	3.1	3.1	3.5	3.5	3.1
$C_d(=\lvert\boldsymbol{\tau}_{btm}\rvert/(\rho_0U_{tide}^2)$ $=u_\tau^2/U_{tide}^2)$ $[\times10^{-3}]$	3.1	2.0	1.9	1.3	1.3	1.7	1.7	1.3
$\delta(=u_\tau/\lvert f+\sigma\rvert)$[m]	32	26	103	404	444	145	48	21
z_m [m]	20	15	30	52	59	41	24	17
ΔH [m]	3.3	3.1	6.4	13.0	14.1	7.5	4.1	3.9
$\Delta\rho$ $[\times10^{-4}\,\mathrm{kg\,m^{-3}}]$	0.97	0.90	4.2	16.7	17.7	5.8	1.6	1.4
ΔU $[\times10^{-2}\,\mathrm{m\,s^{-1}}]$	0.18	0.16	0.62	1.92	2.01	0.69	0.23	0.15
S_ρ $[\times10^{-5}\,\mathrm{kg\,m^{-3}}]$	4.9	4.3	10.8	20.4	22.3	14.7	7.1	5.4
S_w $[\times10^{-4}\,\mathrm{m\,s^{-1}}]$	7.1	7.3	8.2	9.3	9.3	9.3	8.3	8.4
P-term $[\times10^{-4}\ \mathrm{W\ m^{-2}}]$	9.1	4.6	5.4	3.9	4.2	5.3	4.5	3.2
B-term $[\times10^{-6}\ \mathrm{W\ m^{-2}}]$	1.9	1.2	4.8	12.4	15.2	7.5	2.9	1.7
β [%]	0.20	0.25	0.85	3.14	3.50	1.38	0.63	0.51

TABLE 1. Experimental parameters and physical quantities in the experiment. z_m is averaged over the last tidal cycle ($t=47$–48), and the others are averaged over the whole experimental period. $\boldsymbol{\tau}_{btm}$ is the tidal stress at the bottom.

rotates anticlockwise on the tidal ellipse which has a polarization equivalent to Ro_t in cases A to F, whereas it is a unidirectional steady flow in case Ek and a bidirectional oscillating flow in case St (figure 2; see SA08 for details).

The turbulent field in statistical equilibrium obtained after 24 tidal cycles under unstratified condition was used for the initial velocity field after Coleman, Ferziger & Spalart (1992). The initial density field was set linearly stratified as follows:

$$\rho=\rho_z^{init}z+\rho_{btm}^{init}. \tag{2.9}$$

ρ_{btm}^{init} was set to $1.0\times10^{-1}\,\mathrm{kg\,m^{-3}}$ and ρ_z^{init} to $-1.05\times10^{-4}\,\mathrm{kg\,m^{-4}}$, giving the buoyancy frequency $N=\sqrt{-g\rho_z^{init}/\rho_0}=1\times10^{-3}\,\mathrm{s^{-1}}$, which is typical for the polar shelves (e.g. Gordon 1998). For clarity of the experiment, no buoyancy forcing to maintain the stratification such as surface heating was considered.

The Reynolds numbers Re defined by $(H_{tide}U_{tide})/\nu$ ranged from 1000 to 4580 (table 1). Although these values are much smaller than those in the actual ocean based on the molecular viscosity, 'Reynolds number similarity' says that turbulent properties become independent of Re when Re exceeds $O(10^3)$ (Strang & Fernando 2001). We confirmed that turbulent properties were essentially unchanged in an additional experiment for case E with a halved Re of 1250 (e.g. the change of thickness of the formed mixed layer was less than 3 %).

The domain size and grid lengths were determined by using H_{tide} as a unit and then varied among cases in a dimensional form. The horizontal sizes L_x and L_y are 32 in H_{tide} (the dimensional size varies from 38 to 173 m), and the vertical size H is 256 (307 to 1380 m). The horizontal grid lengths Δx and Δy are 0.25 (0.29 to 1.4 m), and the vertical one Δz changes from 0.02 just above the bottom (0.023 to 0.11 m) to 10 near the upper boundary (11.7 to 53.7 m). The horizontal domain size and resolution

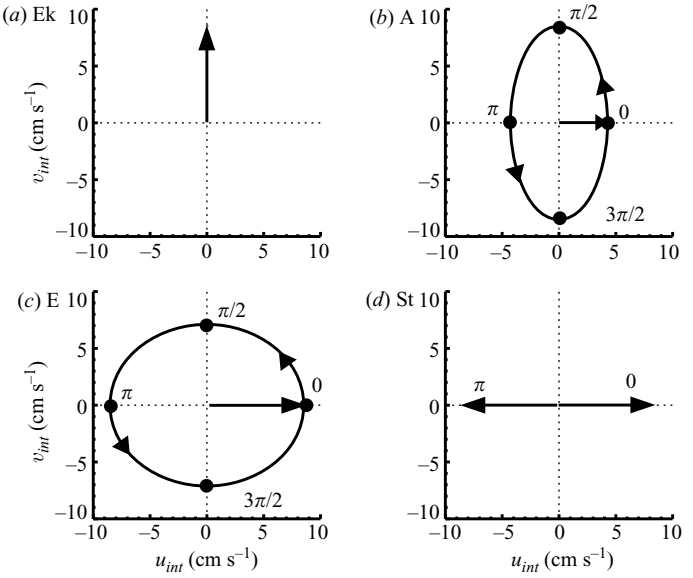

FIGURE 2. The interior flow $\boldsymbol{u}_{int}$ for cases (*a*) Ek, (*b*) A, (*c*) E and (*d*) St. The arrows on the ellipse in (*b*) and (*c*) indicate the direction of rotation, and the numbers in (*b*)–(*d*) the tidal phase.

were halve of those in SA08 in order to save computer resources. It was confirmed in cases A and D that the results hardly changed when the horizontal domain size and resolution were doubled. The method of numerical differentiation and integration of the governing equations is the same as in Akitomo (1999), and briefly explained in SA08. Time integration was carried out for 48 tidal cycles. Hereinafter, the time is counted by tidal cycle.

3. Results

3.1. *Development of the mixed-layer and turbulent properties*

3.1.1. *Turbulence under stratification*

Active turbulent motion and mixing were found in the experiments, as indicated by figure 3 showing distribution of the eddy kinetic energy EKE defined by

$$\mathrm{EKE} = (u'^2 + v'^2 + w'^2)/2, \tag{3.1}$$

where

$$(u', v', w') = (u - \overline{u}^{x,y}, v - \overline{v}^{x,y}, w), \quad \overline{A}^{x,y} = \frac{1}{L_x L_y}\int_0^{L_x}\int_0^{L_y} A \,\mathrm{d}x\,\mathrm{d}y, \tag{3.2}$$

together with the vertical profile of its horizontal average $\overline{\mathrm{EKE}}^{x,y}$, and the density deviation ρ with $\overline{\rho}^{x,y}$ at the end of the experiment ($t = 48$).

As seen in figure 3(*a*), irregular turbulent motion was vigorous for $z < 50\,\mathrm{m}$, and its scale decreased downward like the unstratified experiment (SA08). Corresponding to the flow field, density was homogenized for $z < 50\,\mathrm{m}$, but the initial linear stratification was maintained for $z > 50\,\mathrm{m}$. Thus, the flow was in a laminar state owing to suppression of turbulence for $z > 50\,\mathrm{m}$. Though activity of internal waves is

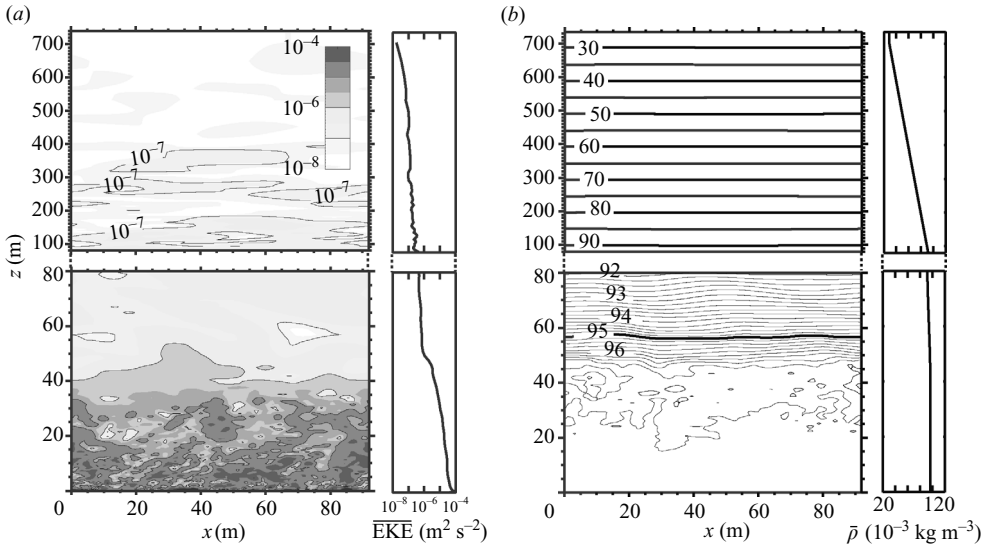

FIGURE 3. (*a*) Vertical section of the eddy kinetic energy EKE at $y = 0$ and $t = 48$ in case E ($Ro_t = 1.2$), together with the vertical profile of the horizontal average $\overline{\mathrm{EKE}}^{x,y}$. Contour lines indicate 10^{-7}, 10^{-6} and $10^{-5}\,\mathrm{m^2\,s^{-2}}$, and darker shades represent larger values. Note that the vertical scale is different for the lower panel showing the range from the bottom ($z = 0$ m) to $z = 80$ m and the upper panel showing from $z = 80$ to 740 m. (*b*) Same as (*a*), but for density ρ. The contour interval of the thin (thick) line is $2.0 \times 10^{-4}\,\mathrm{kg\,m^{-3}}$ ($5.0 \times 10^{-3}\,\mathrm{kg\,m^{-3}}$). The thin contour lines are omitted in the upper panel.

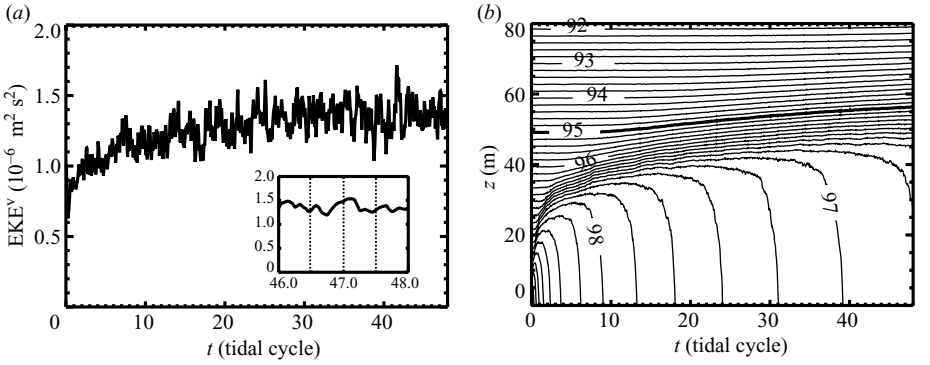

FIGURE 4. Time evolution of (*a*) the areal average of the eddy kinetic energy $\overline{\mathrm{EKE}}^V$ and (*b*) the horizontal averaged density $\overline{\rho}^{x,y}$ in case E. The inset in (*a*) shows $\overline{\mathrm{EKE}}^V$ for $t = 46$–48. The contour interval of (*b*) is $2.0 \times 10^{-4}\,\mathrm{kg\,m^{-3}}$.

suggested by the undulation of isopycnals in this layer, breaking of the waves did not occur and made little contribution to mixing (see the Appendix for details).

Time evolutions of the areal average of the eddy kinetic energy $\overline{\mathrm{EKE}}^V$ defined by

$$\overline{\mathrm{EKE}}^V = \frac{1}{H}\int_0^H \overline{\mathrm{EKE}}^{x,y}\,\mathrm{d}z, \tag{3.3}$$

and $\overline{\rho}^{x,y}$ are shown in figure 4. After the transition to turbulence occurred ($t < 1$), $\overline{\mathrm{EKE}}^V$ gradually increased with time, accompanied by short-term variations

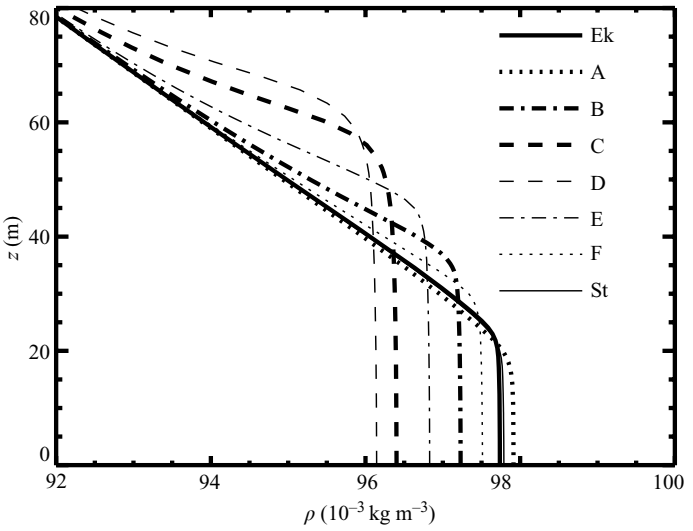

FIGURE 5. The vertical profiles of the horizontal averaged density $\overline{\rho}^{x,y}$ for all cases. The profiles are averaged over the last tidal cycle of the experiments ($t = 47$–48).

(figure 4*a*). This increase corresponded to thickening of the turbulent mixed layer where density was nearly homogenized (figure 4*b*). The homogenized layer developed from ~ 15 m at $t = 1$ to ~ 40 m at $t = 48$. During its development, the layer density decreased from 98.6×10^{-3} kg m^{-3} ($t = 1$) to 96.8×10^{-3} kg m^{-3} ($t = 48$), since the homogenized layer continuously entrained low-density water from above.

The homogenized layer thickness varied significantly among cases, despite the same tidal amplitude U_{tide} (figure 5). The layer became thicker as Ro_t approaches unity, i.e. ~ 17 m in case A ($Ro_t = 0.5$) and ~ 60 m in case D ($Ro_t = 1.05$). This result indicates that the mixing effect in the TBBL was strongly latitude dependent. Under the unstratified condition (SA08), the boundary-layer thickness is decided by the outer length scale $\delta = u_\tau / |f + \sigma|$ (u_τ is frictional velocity), and this is the source of the dependence on Ro_t. Under the stratified condition here, however, the homogenized layer thickness was not proportional to δ, as the ratio of the homogenized layer thickness to δ varied from 0.13 in case D to 0.57 in case A. We will investigate the mechanism leading to this dependence in § 3.2.

3.1.2. *Three-layer structure*

The vertical profiles of physical quantities characterizing turbulence in the boundary layer are shown for case E as a representative case (figure 6). Velocity scale of turbulent motion q, defined by

$$q = \sqrt{\overline{\mathrm{EKE}}^{x,y}}, \tag{3.4}$$

had the maximum near the bottom and decreased with height to below 1×10^{-3} m s^{-1} for $z > 50$ m (figure 6*a*). According to Miles (1986), the gradient Richardson number Ri_g must be below unity in order to maintain turbulence. This condition is applied to the present experiment with

$$Ri_g = -\frac{g}{\rho_0} \frac{\partial \overline{\rho}^{x,y} / \partial z}{(\partial \boldsymbol{u}_{ave} / \partial z)^2}, \tag{3.5}$$

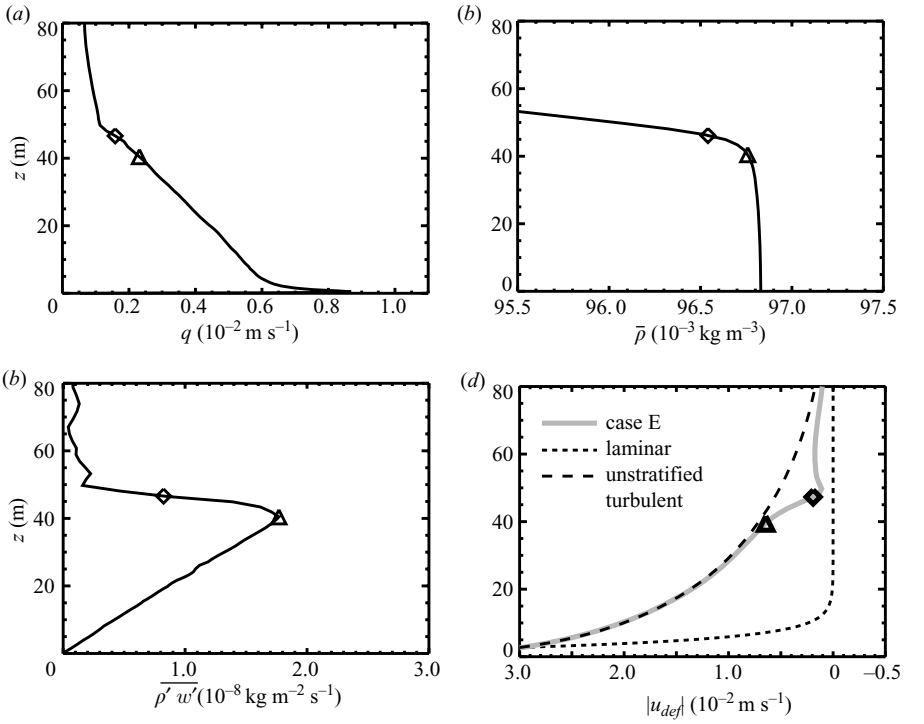

FIGURE 6. The vertical profiles of (*a*) the velocity scale of turbulence q, (*b*) the horizontal averaged density $\overline{\rho}^{x,y}$, (*c*) the turbulent density flux $\overline{\rho' w'}^{x,y}$ and (*d*) the velocity defect of the mean tidal current $|\boldsymbol{u}_{def}|$ (the grey line) in case E. The profiles are averaged over the last tidal cycle of the experiment ($t = 47$–48). △, z_m; ◇, z_t. The short-dashed and long-dashed lines in (*d*) indicate the velocity defects of the laminar and unstratified turbulent tidal flows, respectively.

where the averaged tidal current $\boldsymbol{u}_{ave}$ is

$$\boldsymbol{u}_{ave} = \boldsymbol{u}_{tide} + \overline{u}^{x,y}. \tag{3.6}$$

The height z_t at which $Ri_g = 1$ is indicated by a diamond in figure 6, giving an index of the upper bound of turbulent motion ($q \sim 1 \times 10^{-3}\,\mathrm{m\,s^{-1}}$). ($z_t$ was given by the maximum height that satisfies the condition during $t = 47$–48.)

While the turbulent motion reached z_t, the initial stratification remained with the upper limit of the homogenized layer below z_t (figure 6*b*). Judging from the turbulent density flux $\overline{w'\rho'}^{x,y}$ (figure 6*c*), the upper bound of the homogenized region was located at the height z_m at which $\overline{w'\rho'}^{x,y}$ has the maximum value (indicated by a triangle in figure 6). The height z_m was lower than z_t by 7.5 m in this case. Thus, it can be concluded that the whole water column consists of the three layers: the stratified layer where the initial stratification remains and flow is in a laminar state ($z > z_t$); the mixed layer where density is homogenized by turbulent motion ($z < z_m$); and the interfacial layer where active turbulent motion exists, but the initial stratification remains ($z_m < z < z_t$).

The averaged tidal current showed different features among these three layers, as shown by the vertical profile of the velocity defect $|\boldsymbol{u}_{def}|$ (figure 6*d*) defined by

$$|\boldsymbol{u}_{def}| = |\boldsymbol{u}_{ave} - \boldsymbol{u}_{int}|. \tag{3.7}$$

Note that $|\boldsymbol{u}_{def}|$ was estimated relative to the time-varying $\boldsymbol{u}_{int}$ (see SA08 for details). As seen in figure 6(d), $|\boldsymbol{u}_{def}|$ had the same profile as the unstratified turbulent flow in the mixed layer ($z < z_m$), and it approached the laminar flow (i.e. $\boldsymbol{u}_{tide}$) in the stratified layer ($z > z_t$). In the interfacial layer ($z_m < z < z_t$), as a result, $|\boldsymbol{u}_{def}|$ abruptly changed from the turbulent profile to the laminar one, and the vertical shear was much stronger than that appearing in either turbulent or laminar flow regions.

It has been observed that such a strong shear appears at the top of the bottom mixed layer (Werner *et al.* 2003), showing the interfacial layer in the actual ocean. Laboratory experiments also have shown that the thin interfacial layer accompanied by a strong current shear is formed between the turbulent and laminar regions (Narimousa & Fernando 1987; Fernando 1991), and it has been pointed out that shear instability in this layer is crucial to developing of the mixed layer. Therefore, phenomena occurring in the interfacial layer are a key to the different evolution of the mixed layer among cases (figure 5). They will be investigated in the § 3.2.

3.1.3. *Turbulent properties in the mixed and interfacial layers*

To clarify turbulent properties in the mixed and interfacial layers, velocity and length scales of turbulence, q and l, were evaluated for all cases (figure 7). The length scale l is defined by the standard deviation of density after Tennekes & Lumley (1972), that is,

$$l = \frac{\sqrt{\overline{\rho'^2}^{x,y}}}{(\partial \overline{\rho}^{x,y}/\partial z)}. \tag{3.8}$$

Having the maximum near the bottom, q decreased almost linearly to the top of the mixed layer z_m as shown in figure 6(a) (figure 7a) . Abruptly increasing near the bottom, l maintained its large magnitude at the middle level of the mixed layer and gradually decreased to less than 1 m in the stratified layer (figure 7b).

SA08 examined turbulent properties in the unstratified boundary layer by normalizing them by the frictional velocity u_τ and the length scale $\delta = u_\tau/|f + \sigma|$. Here, normalization with u_τ and z_m is introduced to examine whether q and l in the mixed layer have similarity or not. Figure 8 shows the vertical profiles of q and l, together with those for additional cases E′ and E″ where the tidal amplitude U_{tide} was doubled and halved (17.1 and 4.3 cm s^{-1}), respectively. In the results, both of q/u_τ and l/z_m showed good similarity. After rapidly decreasing from the maximum of ~ 2.5 near the bottom to ~ 1.8 at $z/z_m = 0.1$, q/u_τ showed a gradual decrease to 0.4–0.9 at $z/z_m = 1.0$ (figure 8a). l/z_m increased from nearly zero just above the bottom to 0.2–0.3 at $z/z_m = 0.1$, kept its value for $0.1 < z/z_m < 0.8$, and decreased to 0.1–0.2 near $z/z_m = 1.0$ (figure 8b). This result agrees with the laboratory experiments in the stratified fluid, showing $l/z_m \sim 0.2$ (Stephenson & Fernando 1991).

The situation is somewhat different in the interfacial layer from that in the mixed layer (figure 9). Note that the ordinate in figure 9 is measured by normalized density θ instead of z defined by

$$\theta = -(\overline{\rho}^{x,y} - \overline{\rho}^{x,y}(z_m))/\Delta\rho, \tag{3.9}$$

where $\Delta\rho = \overline{\rho}^{x,y}(z_m) - \overline{\rho}^{x,y}(z_t) > 0$ is the density difference between the top and bottom of the interfacial layer ($\theta = 0$ and 1 correspond to $z = z_m$ and z_t, respectively).

As seen in figure 9(a), q/u_τ was of the order of unity although it somewhat dispersed among cases. This indicates that q is scaled by u_τ as in the mixed layer. The dispersion is attributed to the difference of q/u_τ at $\theta = 0$ ($z = z_m$) which originates from the mixed layer (see figure 8a). Indeed, the vertical change of q/u_τ across the

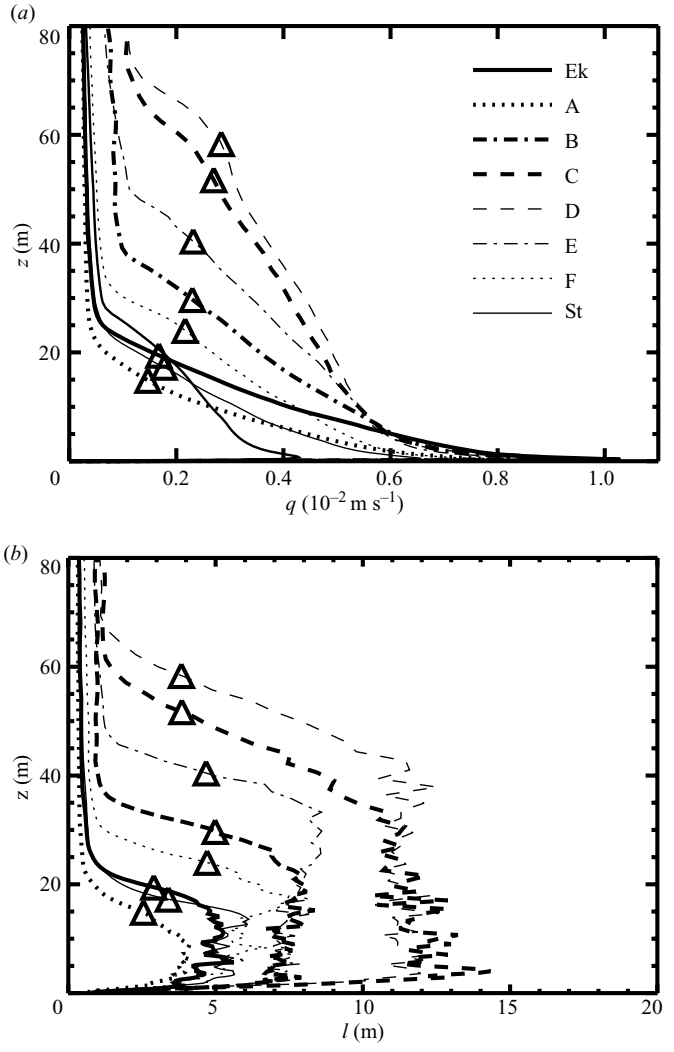

FIGURE 7. The vertical profiles of (*a*) the velocity scale q and (*b*) the length scale l of turbulence for all cases. The profiles are averaged over $t = 47$–48, and the symbols $\triangle$ indicate z_m.

interfacial layer was almost the same among cases, and the profiles of q/u_τ were almost identical for the three cases E, E′ and E″ which have the same conditions but for U_{tide} (u_τ). Then, it can be concluded that q/u_τ has similarity in the interfacial layer, again. On the other hand, the length scale l can be scaled by u_τ/N which is the characteristic length scale of the stratified fluid flow (Nakanishi 2001), and similarity was detected in $l/(u_\tau/N)$, although it slightly dispersed at $\theta \sim 0$ ($z \sim z_m$) again (figure 9*b*).

While the velocity scale q in the interfacial layer is scaled by u_τ as in the mixed layer, the length scale of turbulence l in the interfacial layer is scaled by u_τ/N, not a geometrical scale such as $z_t - z_m$ ($l/(z_t - z_m)$ changed widely from 0.05 to 1.4). The scaling u_τ/N, or q/N, is adopted in turbulent closure models to improve the performance (André *et al.* 1978; Therry & Lacarrère 1983; Galperin *et al.* 1988;

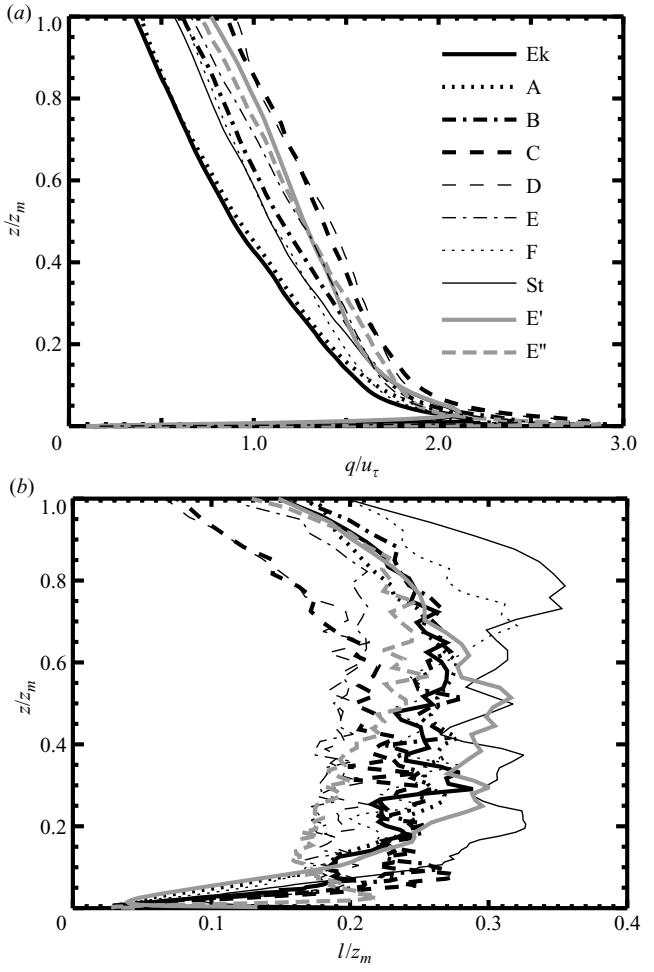

FIGURE 8. The normalized profiles of (*a*) the velocity scale q/u_τ and (*b*) the length scale l/z_m of turbulence in the mixed layer ($0 \leqslant z/z_m \leqslant 1$). The results of the additional experiments of case E′ ($Ro_t = 1.2$, $U_{tide} = 17.1\,\mathrm{cm\,s^{-1}}$) and E″ ($Ro_t = 1.2$, $U_{tide} = 4.3\,\mathrm{cm\,s^{-1}}$) are also shown by the solid and dashed grey lines. The others are the same as figure 7.

Burchard, Petersen & Rippeth 1998; Nakanishi 2001; Nakanishi & Niino 2004), but adequate physical grounds have not been necessarily given by observations or experiments. The present result may provide a basis for the modification of turbulent closure models.

3.2. *Developing mechanism of the mixed layer*

3.2.1. *Conversion of EKE to PE in the interfacial layer*

Development of the turbulent mixed layer is attributed to the conversion of EKE to PE, and the conversion rate has been thought to depend on the production rate of EKE (e.g. Simpson & Hunter 1974). Thus, the rate of energy supply from the tidal current to turbulence was estimated. This rate, called the P-term, was defined by

$$\text{P-term} = -\rho_0 \int_0^H \left\{ \frac{\partial u_{ave}}{\partial z} \overline{u'w'}^{x,y} + \frac{\partial v_{ave}}{\partial z} \overline{v'w'}^{x,y} \right\} \mathrm{d}z, \tag{3.10}$$

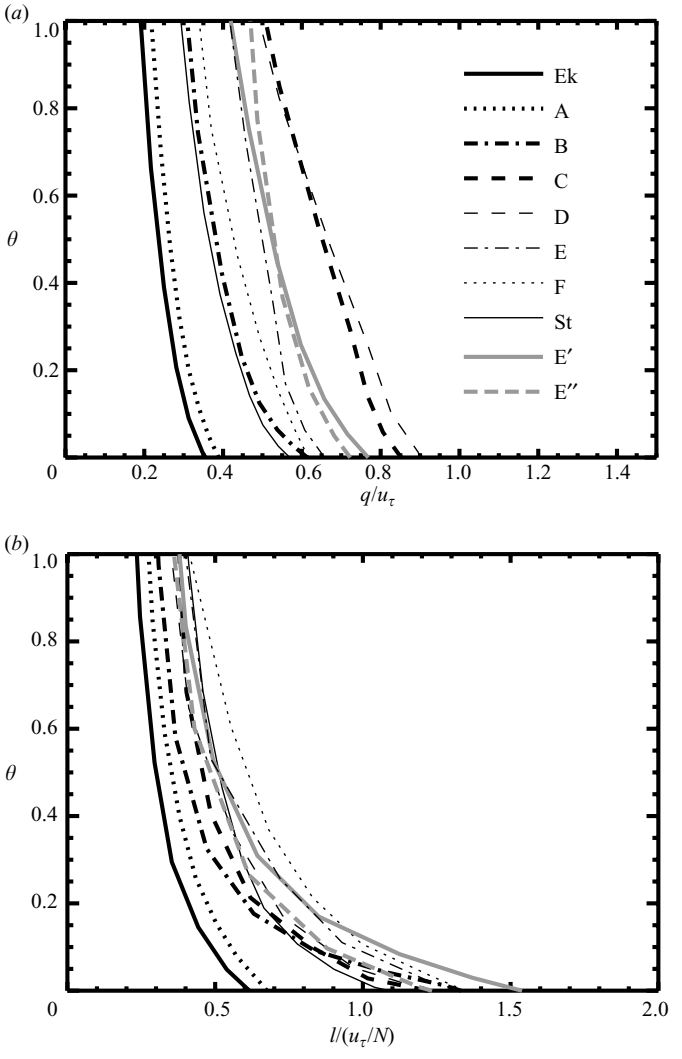

FIGURE 9. Same as figure 8, but for the interfacial layer. The scales q and l are normalized by u_τ and u_τ/N, respectively. The ordinate is $\theta = -(\overline{\rho}^{x,y} - \overline{\rho}^{x,y}(z_m))/\Delta\rho$.

and tabulated for all cases (table 1). The evaluated P-term did not vary much among cases (3.2–$5.4 \times 10^{-4}\,\mathrm{W\,m^{-2}}$) except for case Ek ($9.1 \times 10^{-4}\,\mathrm{W\,m^{-2}}$), and could not explain the difference of the mixed-layer thickness among cases. This is consistent with the fact that the bottom stress (or frictional velocity u_τ) is at the same level except for case Ek owing to the same tidal amplitude U_{tide} (e.g. Fearnhead 1975).

Instead, the conversion rate from EKE to PE, called the B-term, defined by

$$\text{B-term} = g \int_0^H \overline{\rho' w'}^{x,y}\, \mathrm{d}z, \tag{3.11}$$

shows the same dependence on Ro_t as the mixed-layer thickness (z_m). As shown in table 1, the B-term becomes larger as Ro_t approaches unity, 1.2 and $2.9 \times 10^{-6}\,\mathrm{W\,m^{-2}}$ for $Ro_t = 0.5$ and 2.0 (cases A and F), 4.8 and $7.5 \times 10^{-6}\,\mathrm{W\,m^{-2}}$ for $Ro_t = 0.8$ and

1.2 (cases B and E), and 1.2 and 1.5×10^{-5} W m^{-2} for $Ro_t = 0.95$ and 1.05 (cases C and D).

The difference of the B-term among cases is attributed to density deviation ρ', not intensity of turbulent motion w', in the interfacial layer (see (3.11)). Table 1 compares the standard deviations of density $S_\rho = \sqrt{\overline{\rho'^2}^{x,y}}$ and vertical velocity $S_w = \sqrt{\overline{w'^2}^{x,y}}$ in the interfacial layer among cases. The former increased as Ro_t approached unity, but the latter was at the same level in all cases since the intensity of turbulent motion q was at the same level (scaled by u_τ).

The reason why ρ' varied among cases is that the thickness of the interfacial layer $\Delta H (= z_t - z_m \geqslant 0)$ changed depending on Ro_t (table 1). As the initial stratification of $N^2 (= 10^{-6} \mathrm{s}^{-2})$ remains in the interfacial layer, the density jump across the layer $\Delta\rho (= \overline{\rho}^{x,y}(z_m) - \overline{\rho}^{x,y}(z_t) \geqslant 0$ is proportional to ΔH through the approximate relation,

$$\Delta\rho \sim -\overline{\partial\rho/\partial z}\Delta H \sim \frac{\rho_0}{g} N^2 \Delta H, \tag{3.12}$$

and then $\Delta\rho$ increases with ΔH. As shown in table 1, $\Delta\rho$ increased with ΔH although the proportional relation was not detected so clearly. The larger density jump $\Delta\rho$ made density deviation ρ' increase in the interfacial layer. Thus, the B-term increased with ΔH as Ro_t is closer to unity.

The efficiency factor of the energy conversion from EKE to PE, β(= B-term/P-term), is also shown in table 1. Depending on the magnitude of the B-term, β increased from 0.25 % in case A ($Ro_t = 0.5$) to 3.5 % in case D ($Ro_t = 1.05$). The latter is 14 times as large as the former.

3.2.2. *Determination of the interfacial layer thickness*

The gradient Richardson number Ri_g is less than unity in the interfacial layer, whose top is given by $Ri_g = 1$. Therefore, the mean Richardson number Ri_m in the whole interfacial layer, which is given by the velocity jump across the interfacial layer $\Delta U = |u_{def}(z_m) - u_{def}(z_t)|$ and the buoyancy frequency N, should satisfy the following condition,

$$Ri_m = \frac{N^2}{(\Delta U/\Delta H)^2} \leqslant 1. \tag{3.13}$$

This inequality gives the condition for the interfacial layer thickness ΔH as

$$\Delta H \leqslant \Delta U/N. \tag{3.14}$$

As N is almost constant in the interfacial layer (see figure 6*b*), ΔH is bounded above by the magnitude of ΔU. Actually, the experimental results roughly corresponded to the upper bound of (3.14) (figure 10). In cases C and D, the plots of $(\Delta U, \Delta H)$ were located on the right-hand (or down) side of the line of $\Delta H = \Delta U/N$ (the grey line in figure 10). This is probably because stratification in the thick interfacial layer for cases C and D was affected by the lower mixed layer as q and l (figure 9), so that vertical shear of the tidal current $(\partial \boldsymbol{u}_{ave}/\partial z)$ became large as compared to stratification (N). Nevertheless, ΔH was as a whole on the line of $\Delta H = \Delta U/N$. (The proportionality factor of $\Delta H/\Delta U$ averaged among all cases, 0.93×10^3 s, was almost identical to $1/N = 1.0 \times 10^3$ s.) Then, the relationship between ΔH and ΔU is given approximately by

$$\Delta H \sim \Delta U/N. \tag{3.15}$$

The velocity difference ΔU became larger as Ro_t is closer to unity. This is because of the different vertical profiles of the averaged tidal current between laminar and

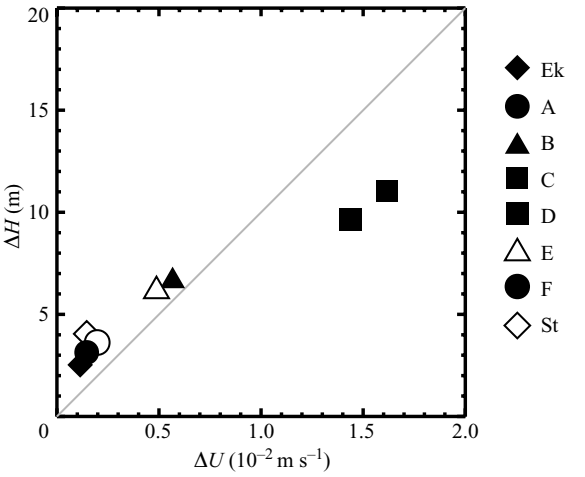

FIGURE 10. The diagram of the velocity jump across the interfacial layer ΔU and the interfacial layer thickness ΔH. Each symbol shows the result averaged over the last tidal cycle ($t = 47$–48). The grey line indicates the relation of $\Delta H = \Delta U/N$.

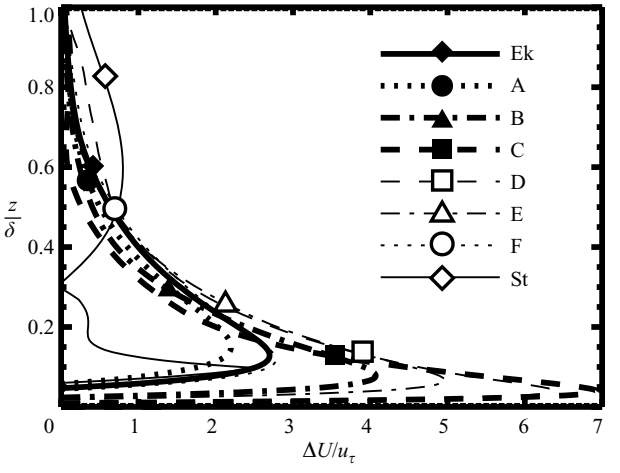

FIGURE 11. The vertical profiles of the difference between the laminar flow (u_{tide}) and the unstratified turbulent flow (Sakamoto & Akitomo 2008) for all cases. (Both of them are shown in figure 6*d* for case E.) The profiles are normalized by the outer scales for the unstratified turbulent flow, i.e. u_τ and δ. Symbols on the lines indicate z_m/δ averaged when $t = 47$–48.

turbulent states (figure 11). Since the vertical scale of the unstratified turbulent boundary layer δ is ten to a hundred times larger than that of the laminar one H_{tide} (table 1), $\Delta U/u_\tau$ has the maximum near the bottom ($z/\delta < 0.15$) in any case, and then decreases with height (less than 0.1 at $z/\delta = 1$). Note that the $\Delta U/u_\tau$ profile does not vary so much for $z/\delta > 0.2$ among cases owing to the similarity of the unstratified boundary layer (SA08). However, the height of the interfacial layer (z_m) was lowered as Ro_t is closer to unity. For example, while the interfacial layer was located at $z_m/\delta = 0.57$ for $Ro_t = 0.5$ (case A), it descended to $z_m/\delta = 0.13$ for $Ro_t = 1.05$ (case D). As a result, ΔU became much larger in the latter case than in the former. This difference is a crucial factor to the different development of the mixed layer among

cases. When the transition to turbulence occurred in the early stage of the experiment, the (laminar) boundary layer reached higher than the height at which $\Delta U/u_\tau$ is a maximum. Then, ΔU monotonically decreased with z after the turbulent flow was set up.

3.3. *Temporal similarity of the mixed-layer development*

Similarity was also found in the time series of the mixed-layer thickness, z_m. Since the mixed layer stops developing when z_m becomes δ (ΔU vanishes), the time scale T_{mix} needed to reach this final state is estimated by dividing the difference of PE between the initial ($z_m = 0$) and final ($z_m = \delta$) states by the energy conversion rate from the tidal current to EKE, the P-term. The difference of PE between the two states is given by,

$$\mathrm{PE} = \int_0^\delta g\frac{\rho_z^{init}\delta}{2}z\,\mathrm{d}z - \int_0^\delta g(\rho_z^{init}z)z\,\mathrm{d}z = -\frac{g\rho_z^{init}\delta^3}{12}, \tag{3.16}$$

where the density gradient ρ_z^{init} is assumed constant (linear stratification), and the P-term is scaled after Simpson & Hunter (1974),

$$\text{P-term} = \rho_0 {u_\tau}^2 U_{tide} = \rho_0 u_\tau^3/\sqrt{C_d}, \tag{3.17}$$

where $C_d = u_\tau^2/U_{tide}^2$ is the drag coefficient (table 1). Thus, T_{mix} is estimated using

$$T_{mix} = \mathrm{PE}/\text{P-term} = \frac{\sqrt{C_d}}{12}\frac{N^2\delta^3}{{u_\tau}^3}. \tag{3.18}$$

T_{mix} represents the time for z_m to reach δ, assuming that the whole EKE supplied from the tidal current is converted to PE. Then it gives the lower bound of the time required for the full development of the mixed layer.

In figure 12(*a*), time evolution of z_m/δ is plotted against the normalized time t/T_{mix} for all cases. All evolutions of z_m/δ were on a universal line, indicating the similarity that the thickness z_m/δ increases with the time t/T_{mix}. Thus, it is interpreted that the difference of the normalized thickness of the mixed layer z_m/δ at a certain dimensional time among cases (figure 11) corresponds to the different stages in the universal evolution. While cases C and D with $Ro_t \sim 1$ are in the early stage with small z_m/δ (small t/T_{mix}), cases A and F with Ro_t far from 1.0 are in the later stage with large z_m/δ (large t/T_{mix}).

The similarity is also found in the time series of ΔU, the B-term and β (figure 12*b–d*). ΔU is large up to $3\times10^{-2}\,\mathrm{m\,s^{-1}}$ at the initial stage with small z_m/δ ($t/T_{mix}\sim10^{-2}$), while it decreases with increase of z_m/δ, and falls below $0.2\times10^{-2}\,\mathrm{m\,s^{-1}}$ at the final stage of the experiments ($t/T_{mix}\sim10^3$). Corresponding to the evolution of ΔU, the interfacial-layer thickness ΔH and the density jump $\Delta\rho$ decrease to nearly zero at large t/T_{mix} (see (3.15) and (3.12); not shown). As a result, the B-term shows a similar decrease (figure 12*c*), and β decreases from 8 % at the initial stage to 0.2 % or less at the final stage (figure 12*d*).

3.4. *Scalings of B-term and β*

It is worth discussing the scalings of the B-term and the efficiency factor β by bulk parameters such as U_{tide} for application to the actual situations. Using the mixing length theory (e.g. Tennekes & Lumley 1972), the turbulent density flux $\overline{\rho' w'}^{x,y}$ is represented in terms of turbulent properties as,

$$\overline{\rho' w'}^{x,y} \sim C_1 q l \frac{\partial \overline{\rho}^{x,y}}{\partial z}, \tag{3.19}$$

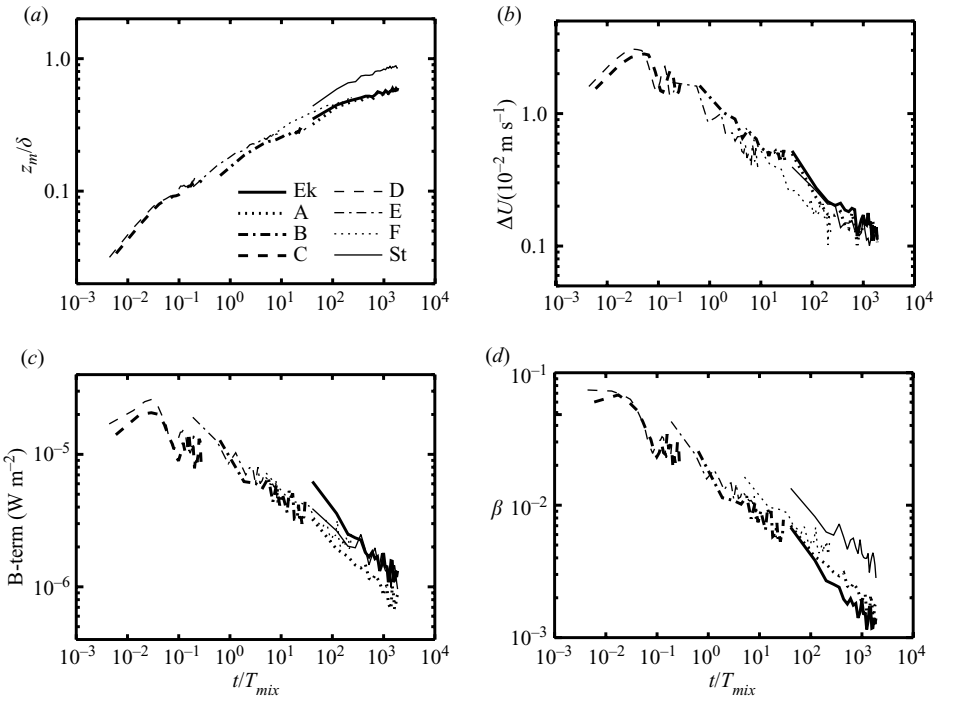

FIGURE 12. Evolution of (*a*) the thickness of the mixed layer z_m/δ, (*b*) the velocity jump across the interfacial layer ΔU, (*c*) the conversion rate from EKE to PE, the B-term, and (*d*) the efficiency factor β. Time t is normalized by the time scale T_{mix}, and the values are averaged every 2 tidal cycles.

where q and l are the velocity and length scales of turbulent eddies, respectively, and C_1 is constant. Since turbulent mixing occurs mainly for $z < z_t$, but $\partial\overline{\rho}^{x,y}/\partial z$ is small for $z < z_m$, the equation obtained by substituting (3.19) into (3.11) can be approximated by

$$\text{B-term} \sim -g\int_{z_m}^{z_t}\left\{C_1 ql\frac{\partial\overline{\rho}^{x,y}}{\partial z}\right\}\mathrm{d}z. \tag{3.20}$$

As shown in figure 9, q and l in the interfacial layer are scaled by u_τ and u_τ/N, respectively, and then $ql \sim C_2 u_\tau^2/N$ where C_2 is constant. Using this relation, (3.20) is converted to

$$\begin{aligned}\text{B-term} &\sim -gCu_\tau^2/N\int_{z_m}^{z_t}\frac{\partial\overline{\rho}^{x,y}}{\partial z}\,\mathrm{d}z\\ &= -gCu_\tau^2/N(\overline{\rho}^{x,y}(z_t)-\overline{\rho}^{x,y}(z_m))\\ &= gC(u_\tau^2/N)\Delta\rho,\end{aligned} \tag{3.21}$$

where $C = C_1C_2$. Thus, the B-term is proportional to the density difference $\Delta\rho$ across the interfacial layer, which is consistent with the experimental results. The constant C is ~ 0.1 based on the experimental results.

Further, using (3.12) and (3.15), (3.21) can be written as a function of ΔU as

$$\text{B-term} \sim \rho_0 Cu_\tau^2\Delta U. \tag{3.22}$$

ΔU is the difference of the mean tidal current across the interfacial layer, and is approximated to

$$\Delta U = |\boldsymbol{u}_{def}(z_m) - \boldsymbol{u}_{def}(z_t)| \sim |\boldsymbol{u}_{def}(z_m)|, \tag{3.23}$$

since $\boldsymbol{u}_{def}(z_t)$ in the laminar stratified layer is small compared to $\boldsymbol{u}_{def}(z_m)$ in the turbulent mixed layer (e.g. figure 6*d*). As a result, using the relation $u_\tau = \sqrt{C_d}U_{tide}$, (3.22) is given by

$$\text{B-term} \sim \rho_0 C u_\tau^2 |\boldsymbol{u}_{def}(z_m)| = \rho_0 C C_d^{3/2} U_{tide}^3 (|\boldsymbol{u}_{def}(z_m)|/u_\tau). \tag{3.24}$$

Together with P-term $\sim \rho_0 u_\tau^2 U_{tide}$, this equation gives an approximate relation between β and properties of the tidal current,

$$\beta = \text{B-term/P-term} \sim C|\boldsymbol{u}_{def}(z_m)|/U_{tide} = C\sqrt{C_d}(|\boldsymbol{u}_{def}(z_m)|/u_\tau). \tag{3.25}$$

If the bottom drag coefficient C_d is approximated to be constant (table 1), the B-term is determined by z_m/δ and the tidal amplitude U_{tide} from (3.24) and β by only z_m/δ from (3.25), since the vertical structure of $|\boldsymbol{u}_{def}(z/\delta)|/u_\tau$ has similarity (SA08).

3.5. *Entrainment velocity and turbulent diffusivity*

Many studies investigated the entrainment process by laboratory experiments with a two-layer fluid with density jump $\Delta\rho$ (e.g. Moore & Long 1971; Narimousa & Fernando 1987; Fernando 1991). According to them, the entrainment velocity u_e depends on the bulk Richardson number Ri_b defined with the velocity jump between the two layers ΔU, that is,

$$Ri_b = \frac{\Delta\rho g z_m}{\rho_0 \Delta U^2}, \tag{3.26}$$

and it has been reported that u_e is in inverse proportion to Ri_b when $Ri_b = 1$–10, which corresponds to our cases.

To confirm this relationship, the entrainment velocity $u_e = \mathrm{d}z_m/\mathrm{d}t$ was plotted against Ri_b , which was estimated using averaged values of z_m $\Delta\rho$, and ΔU over 8 tidal cycles (6 values for each case; figure 13). Despite somewhat dispersive, u_e/U_{tide} decreased with Ri_b and the regression line (the solid line in figure 13) was obtained as

$$u_e/U_{tide} = 3.7 \times 10^{-4} Ri_b^{-1.1}. \tag{3.27}$$

Though the coefficient 3.7×10^{-4} is rather small compared with previous studies, the dependence on the bulk Richardson number, $u_e \propto Ri_b^{-1.1}$, almost coincides with $u_e \propto Ri_b^{-1}$ obtained previously (e.g. Moore & Long 1971; Narimousa & Fernando 1987; Fernando 1991). Kato & Phillips (1969) pointed out that this relation holds true when shear instability in the interfacial layer controls the mixed-layer development, and this is also consistent with the present results.

Equation (3.27) appears inconsistent with the result that the mixed layer develops faster as $\Delta\rho$ increases. This discrepancy is easily resolved by considering that ΔU is proportional to $\Delta\rho$. Supposing for simplicity, that u_e is proportional to Ri_b^{-1} the following relation is derived from (3.12) and (3.15),

$$u_e \propto Ri_b^{-1} \propto \Delta U^2/\Delta\rho \propto \Delta\rho. \tag{3.28}$$

This relation is consistent with the result obtained in the previous section.

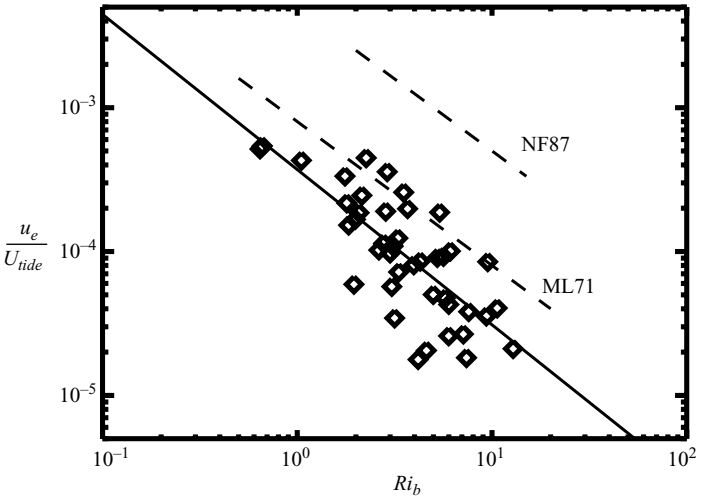

FIGURE 13. The diagram of the normalized entrainment velocity u_e/U_{tide} and the bulk Richardson number $Ri_b = \Delta\rho g z_m/(\rho_0 \Delta U^2)$. The diamonds indicate the values obtained by averaging the time series of the experimental results every 8 tidal cycles for all cases. The solid line indicates the regression line of $u_e/U_{tide} = 3.7 \times 10^{-4} Ri_b^{-1.1}$, and the dashed lines show the results of Moore & Long (1971) (ML71) and Narimousa & Fernando (1987) (NF87).

To evaluate turbulent mixing in the mixed layer quantitatively, the apparent diffusivity κ_{ap}, which was estimated by

$$-\kappa_{ap} \frac{\mathrm{d}\overline{\rho}^{x,y}}{\mathrm{d}z} = \overline{\rho' w'}^{x,y}, \tag{3.29}$$

is shown in figure 14. As Ro_t approached unity, the maximum κ_{ap} increased and the layer with large κ_{ap} thickened (figure 14*a*). While κ_{ap} was 0.003 $\mathrm{m^2\ s^{-1}}$ at the maximum in case A, it reached 0.013 $\mathrm{m^2\ s^{-1}}$ in case D (0.024 $\mathrm{m^2\ s^{-1}}$ in the additional case E′ with U_{tide} doubled). A similar value of eddy diffusivity ($>0.01\ \mathrm{m^2\ s^{-1}}$) was reported at the shelf break of the Weddell Sea (Pereira, Beckmann & Hellmer 2002). Normalized diffusivity, $\kappa_{ap}/(u_\tau z_m)$, showed similarity again (figure 14*b*). The maximum was located at $z/z_m \sim 0.3$. This structure coincides with the result of SA08 though the maximum value of $0.06 \sim 0.08$ is nearly twice as large as that in SA08 ($\sim$0.04).

4. Conclusions and discussion

To investigate turbulent properties and the developing mechanisms of the tidally induced bottom boundary layer under stratification, non-hydrostatic three-dimensional model experiments were executed in the linearly stratified rotating ocean. The following conclusions were obtained based on eight experimental cases with different temporal Rossby number $Ro_t = |\sigma/f|$, the ratio of the tidal frequency σ to the Coriolis parameter f. Figure 15 gives the schematic view about the dynamics of the turbulent TBBL under stratification.

During the development of the mixed layer, the whole water column has the three-layer structure: the mixed layer where density is homogenized and the flow is turbulent ($z < z_m$), the stratified layer where the initial stratification remains and the flow is laminar ($z > z_t$), and the interfacial layer between them where the flow is turbulent, but the stratification remains ($z_m < z < z_t$). The upper bound of the mixed

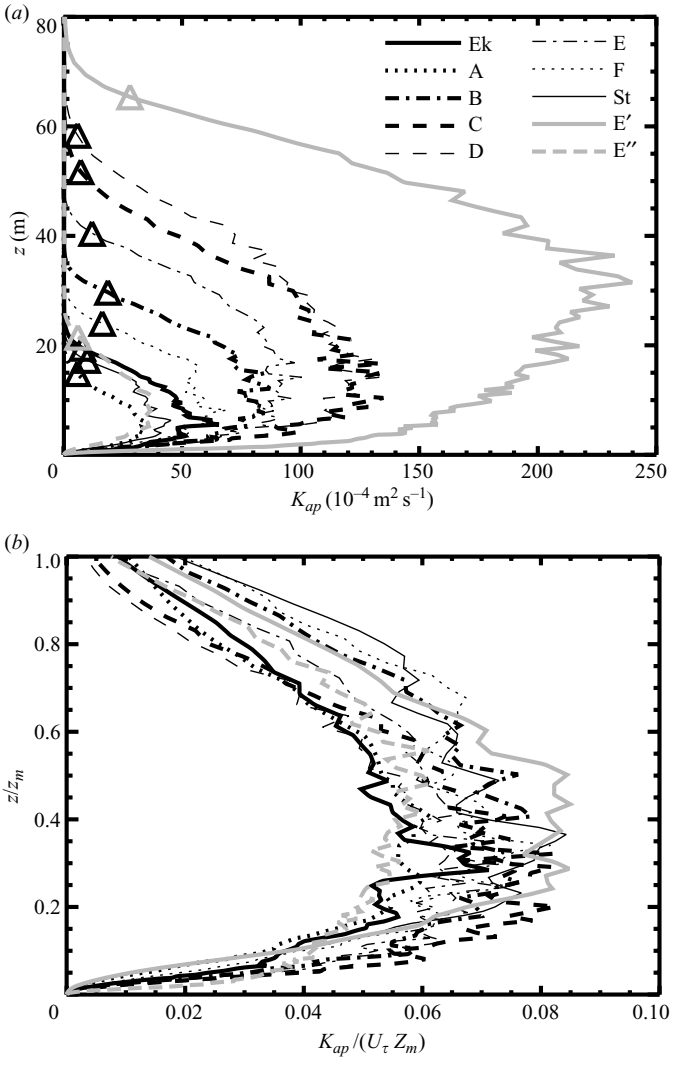

FIGURE 14. (*a*) Dimensional ($0 < z < 80$ m) and (*b*) non-dimensional ($0 < z/z_m < 1.0$) vertical profiles of the apparent diffusivity κ_{ap}. The profiles are averaged over the last tidal cycle of the experiments ($t = 47$–48), and the additional cases E′ and E″ are also shown by grey lines.

layer is given by the height where the upward density flux has the maximum (z_m), and that of the interfacial layer is determined by the height where the gradient Richardson number becomes unity (z_t). The mean tidal flow in the mixed layer has the same vertical profile as in the unstratified turbulent tidal flow, while that in the stratified layer has the same profile as in the laminar tidal flow. As a result, strong vertical shear is formed in the interfacial layer.

The velocity scale of turbulence q is scaled by the frictional velocity u_τ both in the mixed and interfacial layers. On the other hand, the length scale l is scaled by z_m in the mixed layer and by u_τ/N in the interfacial layer where the initial stratification still remains. The vertical profiles of q and l normalized by these scaling quantities have similarity in each layer.

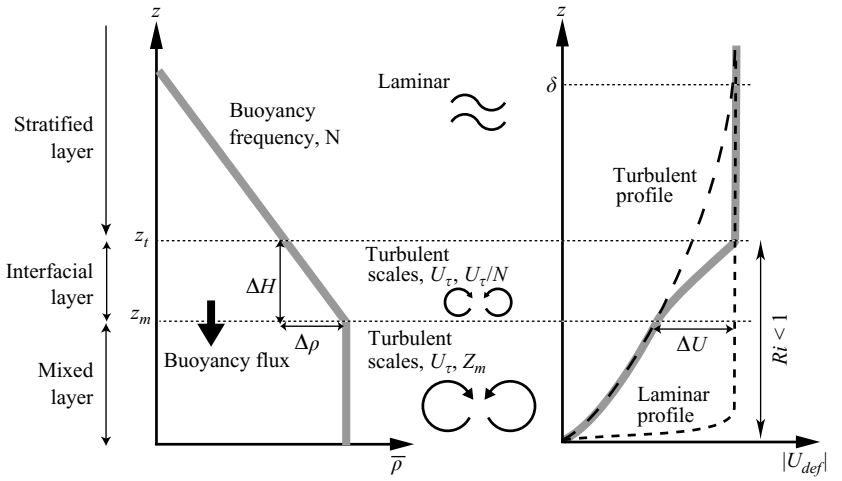

FIGURE 15. A schematic view of the three-layer structure of the water column and the mechanism of the mixed-layer development. The left- and right-hand grey lines indicate the vertical profiles of the averaged density and tidal current, respectively.

Even when the background tidal current has the same amplitude U_{tide} (or the energy conversion rate from the background tidal current to the eddy kinetic energy, the P-term, is unchanged), the mixed layer develops more rapidly as Ro_t is closer to unity. This is because the energy conversion rate from the eddy kinetic energy to the potential energy (the B-term) increases as Ro_t approaches unity.

The difference of the B-term among cases is induced by different velocity shears formed in the interfacial layer. As Ro_t approaches unity, the shear becomes stronger since the velocity gap between the turbulent flow in the mixed layer and the laminar flow in the stratified layer increases. The larger velocity gap leads to the thicker interfacial layer, and then density deviation becomes larger within the layer to enhance the B-term.

The time evolution of the normalized mixed-layer thickness z_m/δ has similarity against the normalized time t/T_{mix}, where T_{mix} is the time scale required for the mixed layer to thicken up to the boundary-layer thickness of an unstratified fluid $\delta = u_\tau/|f+\sigma|$. From this viewpoint of similarity, the different thickness z_m of the mixed layer at a certain dimensional time among cases corresponds to the different stage in the universal time evolution of the mixed layer. The B-term and the efficiency factor β (= B-term/P-term) also has similarity. The magnitude of β decreases from about 8 % at the initial stage to less than 0.1 % at the final stage. A universal formulation of β may be possible based on this time similarity.

The entrainment velocity u_e is nearly in inverse proportion to the bulk Richardson number defined by $Ri_b = g\Delta\rho z_m/\rho_0\Delta U^2$, (i.e. $u_e/U_{tide} \sim 3.7\times10^{-4}Ri_b^{-1.1}$). This almost coincides with the relationship derived from laboratory experiments with a two-layer shear flow, $u_e \propto Ri_b^{-1}$ (e.g. Fernando 1991). The apparent diffusivity κ_{ap} in the mixed layer also has similarity as in the unstratified case (SA08). The dimensional value increases with Ro_t, its maximum evaluated at $0.003\,\mathrm{m^2\,s^{-1}}$ ($Ro_t = 0.5$) to $0.013\,\mathrm{m^2\,s^{-1}}$ ($Ro_t = 1.05$).

In this study, the experiments with $Ro_t = 0.95$ and 1.05 (cases C and D) were used for the cases close to the critical latitude. However, discussion of the situation where Ro_t is closer to unity is meaningful for speculating about tidal mixing in the regions

adjacent to the critical latitude. In the situation, it is expected that, as compared to cases C and D, z_m/δ is further lowered due to increase of δ, and that the velocity gap in the interfacial layer becomes larger as suggested by the vertical profiles of $\Delta U/u_\tau$ for cases C and D (figure 11). This indicates formation of the thick interfacial layer, although deviation from the approximate relation $\Delta H = \Delta U/N$ may increase (figure 10). Thus, it is likely that more active mixing than in cases C and D will occur when $0.95 < Ro_t < 1.05$.

Since we considered the simple situation of the tidal pressure gradient oscillating in one direction, the background tidal currents rotate anticlockwise corresponding to $f < 0$ in all cases (figure 2). However, oscillation of the tidal pressure gradient is complicated in the real ocean, so that the tidal ellipse can be clockwise in some regions. In that case, $\delta = u_\tau/|f + \sigma|$ remains small even when Ro_t is close to unity, since the clockwise tidal ellipse corresponds to $\sigma < 0$ as discussed in SA08 (while $\sigma > 0$ for anticlockwise). For example, while δ is up to 440 m for the anticlockwise tidal ellipse with $Ro_t = 1.05$ (case D), δ is only 10 m for the clockwise ellipse, which indicates that mixing would be weaker than case A of $Ro_t = 0.5$ ($\delta = 26$ m). This dependence of the mixing effect on the tidal ellipse (polarization) is consistent with the result of Makinson (2002).

The continental shelf break region of the Weddell Sea, which is located near the critical latitude of the semi-diurnal tides, is a major site of bottom water formation. There, cold dense shelf water (ice shelf water) is mixed with a warm water mass penetrating into the shelf (modified warm deep water), to form the water that flows off the shelf and downslope (Foster *et al.* 1987; Gordon 1998; Foldvik *et al.* 2004). Although it has been pointed out that many factors are related to the mixing process, e.g. breaking of internal waves excited on shelf slopes, double-diffusive convection, and turbulence generated by surface dynamics such as ice movement or storms, turbulent mixing in the TBBL is expected to be an important process in determining the properties of the bottom water (Foster *et al.* 1987; Robertson 2001*a*, *b*; Pereira *et al.* 2002). Actually, observations and numerical simulations have shown that vertical shear of the anticlockwise tidal currents reaches several hundreds of metres above the bottom (Foldvik *et al.* 1990; Robertson 2001*a*; Pereira, Beckmann & Hellmer 2002). Further, Makinson *et al.* (2006) showed that there is a strong tidal current shear between the mixed boundary layer and the stratified interior. These facts strongly suggest active mixing in the TBBL according to the present results.

It is worth discussing the performance of turbulent closure models based on the present result. The MY scheme estimates the mixing effect using q and l (Mellor & Yamada 1982). While q is forecast in the model, the determination of l is somewhat ambiguous (Nakanishi 2001). However, the present study clearly shows that the length scale l is given by q/N in the interfacial layer. Recent studies have modified the MY scheme in a similar way and obtained better performances (Burchard, Petersen & Rippeth 1998; Nakanishi 2001; Nakanishi & Niino 2004). In addition, as Werner *et al.* (2003) suggested, the critical gradient Richardson number Ri_{gc} may be larger (1.0 or so) than 0.19 which is adopted in the original MY scheme. The KPP scheme (the K profile parameterization; Durski, Glenn & Haidvogel 2004; Large, McWilliams & Doney 1994), another mixed layer scheme giving good performances, may suffer similar shortcomings in reproducing the interfacial layer, since l is given by an empirical vertical shape function and q is assumed to be constant except in the vicinity of the bottom.

The efficiency factor of the energy conversion from EKE to PE, β, is an important issue for the mixed-layer development or the turbulent mixing process in the actual

Case	Ek	A	B	C	D	E	F	St
$Ro_t = \lvert\sigma/f\rvert$	0	0.5	0.8	0.95	1.05	1.2	2.0	∞
EKE flux [$\times 10^{-7}$ W m^{-2}]	1.3	1.0	0.86	2.2	1.1	0.62	0.28	1.6

TABLE 2. Upward energy flux estimated at $z = 80$ m and averaged over the whole experimental period.

ocean. The previous estimation of β based on observation varies on the wide range of 0.28–14 % (Fearnhead 1975; Schumacher *et al.* 1979; Bowman 1980; Yanagi & Ohba 1985), and does not exhibit the dependence on latitude which is suggested in the present experiment. Apart from these values being indirectly estimated, many factors such as coastal terrain, bottom topography, surface heating, freshwater input, interactions of multi-tidal constituents may play some role in determining the value of β. In addition, polarization of the tidal ellipse might have some relationship to the change of β as discussed above. Though it is necessary to take account of these various factors for further understanding of the tidal mixing process and formulation of the mixing effect in the actual ocean, we believe that the present results serve as a foundation for future work.

The authors wish to express their thanks to T. Awaji, M. Konda and Y. Ishikawa for helpful discussion throughout this study. Numerical calculations were carried out on PRIMEPOWER HPC2500 at the Academic Center for Computing and Media Studies of Kyoto University. The research was partly supported by the Sasakawa Scientific Research Grant from The Japan Science Society.

Appendix. Effects of internal waves

In the present experiments, perturbations existed even in the interior region where no turbulent motion was observed (e.g. figure 3). These perturbations are thought to be internal gravity waves excited by turbulence in the boundary layer (or initial shocks due to the experimental settings) since the vertical transport of EKE nearly coincided with the theory of internal waves. According to previous studies, when the interior region is continuously stratified, EKE is removed by internal waves so that the mixing is weakened in the boundary layer (e.g. Kantha, Phillips & Azad 1977). However, the upward EKE flux at $z = 80$ m was only 2×10^{-8} to 3×10^{-7} W m^{-2} here (table 2), which were less than 0.1 % of the whole energy supply to EKE (P-term), and less than 10 % of the energy conversion from EKE to PE (B-term). Thus, internal waves have little influence on the mixing-layer development in the present experiment even if the energy put into internal waves are all converted into PE.

There is another possibility that the EKE transported upward by internal waves may make a contribution to the mixing process in the interior region. However, the apparent diffusivity estimated in the interior region was less than 10^{-6} m^2 s^{-1} and therefore negligible.

REFERENCES

AELBRECHT, D., D'HIERES, G. C. & RENOUARD, D. 1999 Experimental study of the Ekman layer instability in steady or oscillating flows. *Continental Shelf Res.* **19**, 1851–1867.

AKHAVAN, R., KAMM, R. D. & SHAPIRO, A. H. 1991 An investigation of transition to turbulence in bounded oscillatory Stokes flows. Part 2. Numerical simulations. *J. Fluid Mech.* **225**, 423–444.

Akitomo, K. 1999 Open-ocean deep convection due to thermobaricity 2. Numerical experiments. *J. Geophys. Res.* **104**, 5235–5249.

André, J. C., Moor, G. D., Lacarrère, P., Therry, G. & Vachat, R. D. 1978 Modeling the 24-hour evolution of the men and turbulent structures of the planetary boundary layer. *J. Atmos. Sci.* **35**, 1861–1883.

Baines, P. G. & Condie, S. 1998 Observations and modelling of Antarctic downslope flows: a review. *Antarct. Res. Ser.* **75**, 29–49.

Bowman, M. J. 1980 M2 tidal effects in Greater Cook Strait, New Zealand. *J. Geophys. Res.* **85**, 2728–2742.

Burchard, H. 2001 On the q^2l equation by Mellor and Yamada (1982). *J. Phys. Oceanogr.* **31**, 1377–1387.

Burchard, H., Petersen, O. & Rippeth, T. P. 1998 Comparing the performance of the Mellor–Yamada and the k–ϵ two-equation turbulence models. *J. Geophys. Res.* **103**, 10 543–10 554.

Chen, D., Ou, H. W. & Dong, C. 2003 A model study of internal tides in coastal frontal zone. *J. Phys. Oceanogr.* **33**, 170–187.

Chen, R. T., Ling, C. & Gartner, J. W. 1999 Estimates of bottom roughness length and bottom shear stress in South San Francisco Bay, California. *J. Geophys. Res.* **104**, 7715–7728.

Coleman, G. N. 1999 Similarity statistics from a direct numerical simulation of the neutrally stratified planetary boundary layer. *J. Atmos. Sci.* **56**, 891–900.

Coleman, G. N., Ferziger, J. H. & Spalart, P. R. 1992 Direct simulation of the stably stratified turbulent Ekman layer. *J. Fluid Mech.* **244**, 677–712.

Durski, S. M., Glenn, S. M. & Haidvogel, D. B. 2004 Vertical mixing schemes in the coastal ocean: comparison of the level 2.5 Mellor–Yamada scheme with an enhanced version of the K profile parameterization. *J. Geophys. Res.* **109**, C04015.

Fearnhead, P. G. 1975 On the formation of fronts by tidal mixing around the British Isles. *Deep-Sea Res.* **22**, 311–321.

Fernando, H. J. S. 1991 Turbulent mixing in stratified fluids. *Annu. Rev. Fluid Mech.* **23**, 455–493.

Foldvik, A., Middleton, J. H. & Foster, T. D. 1990 The tides of the southern Weddell Sea. *Deep-Sea Res.* **37**, 1345–1362.

Foldvik, A., Gammelsrød, T., Østerhus, S., Fahrbach, E., Rohardt, G., Schröder, M., Nicholls, K. W., Padman, L. & Woodgate, R. A. 2004 Ice shelf water overflow and bottom water formation in the southern Weddell Sea. *J. Geophys. Res.* **109**, C02015.

Foster, T. D. & Carmack, E. C. 1976 Frontal zone mixing and Antarctic Bottom Water formation in the southern Weddell Sea. *Deep-Sea Res.* **23**, 301–317.

Foster, T. D., Foldvik, A. & Middleton, J. H. 1987 Mixing and bottom water formation in the shelf break region of the southern Weddell Sea. *Deep-Sea Res.* **34**, 1771–1794.

Furevik, T. & Foldvik, A. 1996 Stability at M(2) critical latitude in the Barents Sea. *J. Geophys. Res.* **101**, 8823–8837.

Galperin, B., Kantha, L. H., Hassid, S. & Rosati, A. 1988 A quasi-equilibrium turbulent energy model for geophysical flows. *J. Atmos. Sci.* **45**, 55–62.

Gordon, A. L. 1998 Western Weddell Sea thermohaline stratification. Ocean, ice and atmosphere: interactions at the Antarctic continental margin. *Antarct. Res. Ser.* **75**, 215–240.

Guo, X. & Valle-Levinson, A. 2007 Tidal effects on estuarine circulation and outflow plume in the Chesapeake Bay. *Continental Shelf Res.* **27**, 20–42.

Kantha, L. H., Phillips, O. M. & Azad, R. S. 1977 On turbulent entrainment at a stable density interface. *J. Fluid Mech.* **79**, 753–768.

Kato, H. & Phillips, O. M. 1969 On the penetration of a turbulent layer into stratified fluid. *J. Fluid Mech.* **37**, 643–655.

Killworth, P. D. & Edwards, N. R. 1999 A turbulent bottom boundary layer code for use in numerical ocean models. *J. Phys. Oceanogr.* **29**, 1221–1238.

Large, W. G., McWilliams, J. C. & Doney, S. C. 1994 Oceanic vertical mixing: a review and a model with a nonlocal boundary layer parameterization. *Rev. Geophys.* **32**, 363–403.

Li, M., Zhong, L. & Boicourt, W. C. 2005 Simulations of Chesapeake Bay estuary: sensitivity to turbulence mixing parameterizations and comparison with observations. *J. Geophys. Res.* **110**, C12004.

Makinson, K. 2002 Modeling tidal current profiles and vertical mixing beneath Filchner–Ronne Ice Shelf, Antarctica. *J. Phys. Oceanogr.* **32**, 202–215.

Makinson, K., Schröder, M. & Østerhus, S. 2006 Effect of critical latitude and seasonal stratification on tidal current profiles along Ronne Ice Front, Antarctica. *J. Geophys. Res.* **111**, C03022.

Mellor, G. L. & Yamada, T. 1982 Development of a turbulence closure model for geophysical fluid problems. *Rev. Geophys. Space Phys.* **20**, 851–875.

Miles, J. 1986 Richardson's criterion for the stability of stratified shear flow. *Phys. Fluids* **29**, 3470–3471.

Moore, M. J. & Long, R. R. 1971 An experimental investigation of turbulent stratified shearing flow. *J. Fluid Mech.* **49**, 635–655.

Nakanishi, M. 2001 Improvement of the Mellor–Yamada turbulence closure model based on large-eddy simulation data. *Boundary-Layer Met.* **99**, 349–378.

Nakanishi, M. & Niino, H. 2004 An improved Mellor–Yamada level-3 model with condensation physics: its design and verification. *Boundary-Layer Met.* **112**, 1–31.

Nakano, H. & Suginohara, N. 2002 Effects of bottom boundary layer parameterization on reproducing deep and bottom waters in a world ocean model. *J. Phys. Oceanogr.* **32**, 1209–1227.

Narimousa, S. & Fernando, H. J. S. 1987 On the sheared density interface of an entraining stratified fluid. *J. Fluid Mech.* **174**, 1–22.

Nimmo Smith, W. A. M., Katz, J. & Osborn, T. R. 2005 On the structure of turbulence in the bottom boundary layer of the coastal ocean. *J. Phys. Oceanogr.* **35**, 72–93.

Nost, E. 1994 Calculating tidal current profiles from vertically integrated models near the critical latitude in the Barents Sea. *J. Geophys. Res.* **99**, 7885–7901.

Nunes Vaz, R. A. & Simpson, J. H. 1994 Turbulence closure modeling of estuarine stratification. *J. Geophys. Res.* **99**, 16143–16160.

Pereira, F. P., Beckmann, A. & Hellmer, H. H. 2002 Tidal mixing in the southern Weddell Sea: Results from a three-dimensional model. *J. Phys. Oceanogr.* **32**, 2151–2170.

Robertson, R. 2001*a* Internal tides and baroclinicity in the southern Weddell Sea 1. Model description. *J. Geophys. Res.* **106**, 27 001–27 016.

Robertson, R. 2001*b* Internal tides and baroclinicity in the southern Weddell Sea 2. Effects of the critical latitude and stratification. *J. Geophys. Res.* **106**, 27 017–27 034.

Robertson, R. 2005 Baroclinic and barotropic tides in the Weddell Sea. *Antarct. Sci.* **17**, 461–474.

Sakamoto, K. & Akitomo, K. 2006 Instabilities of the tidally induced bottom boundary layer in the rotating frame and their mixing effect. *Dyn. Atmos. Oceans* **41**, 191–211.

Sakamoto, K. & Akitomo, K. 2008 The tidally induced bottom boundary layer in the rotating frame: similarity of turbulence. *J. Fluid Mech.* **615**, 1–25.

Schumacher, D., Kinder, T. H., Pashinski, D. J. & Charnell, R. L. 1979 A structural front over the continental shelf of the Eastern Bering Sea. *J. Phys. Oceanogr.* **9**, 79–87.

Simpson, J. H. & Hunter, J. R. 1974 Fronts in the Irish Sea. *Nature* **250**, 404–406.

Stephenson, P. W. & Fernando, H. J. S. 1991 Turbulence and mixing in a stratified shear flow. *Geophys. Astrophys. Fluid Dyn.* **59**, 147–164.

Strang, E. J. & Fernando, H. J. S. 2001 Entrainment and mixing in stratified shear flows. *J. Fluid Mech.* **428**, 349–386.

Tennekes, H. & Lumley, J. L. 1972 *A First Course in Turbulence*. The MIT Press.

Therry, G. & Lacarrère, P. 1983 Improving the eddy kinetic energy model for planetary boundary layer description. *Boundary-Layer Met.* **25**, 63–88.

Warner, J. C., Geyer, W. R. & Lerczak, J. Aw. 2005 Numerical modeling of an estuary: A comprehensive skill assessment. *J. Geophys. Res.* **110**, C05001.

Werner, S. R., Beardsley, R. C., Lentz, S. J., Hebert, D. L. & Oakey, N. S. 2003 Observations and modelling of the tidal bottom boundary layer on the southern flank of Georges Bank. *J. Geophys. Res.* **108**, C118005.

Whitworth III, T., Orsi, A. H., Kim, S.–J., Norlin, W. D. & Locarnini, R. A. 1998 Water masses and mixing near the Antarctic slope front. *Antarct. Res. Ser.* **75**, 1–27.

Yanagi, T. & Koike, T. 1987 Seasonal variation in thermohaline and tidal fronts, Seto Inland Sea, Japan. *Continental Shelf Res.* **7**, 149–160.

Yanagi, T. & Ohba, T. 1985 A tidal front in the Bungo Channel. *Bull. on Coastal Oceanogr.* **23**, 19–25.